Chemical Engineering Journal 429 (2022) 132350

Contents lists available at ScienceDirect

Chemical Engineering Journal

journal homepage: www.elsevier.com/locate/cej

Synergistic dual-functionalities of starch-grafted-styrene hydrophilic porous resin for efficiently removing bisphenols from wastewater

Wenjing Yuan [a], Liqin Zhou [a], Zhaoqiang Zhang [b], Yunpan Ying [b], Weidong Fan [b], Kungang Chai [a,*], Ziqi Zhao [a], Zhongwei Tan [a], Fang Shen [a], Hongbing Ji [a,c,*]

[a] School of Chemistry and Chemical Engineering, Guangxi Key Laboratory of Petrochemical Resource Processing and Process Intensification Technology, Guangxi University, Nanning 530004, PR China
[b] Department of Chemical and Biomolecular Engineering, National University of Singapore, 4 Engineering Drive 4, 117585 Singapore
[c] Fine Chemical Industry Research Institute, School of Chemistry, Sun Yat-sen University, Guangzhou 510275, PR China

ARTICLE INFO

Keywords:
Adsorption
Bisphenols
Hypercrosslinked polymer
Hydrophilic
Starch

ABSTRACT

Highly efficient remediation of bisphenols (BPs) contaminated wastewater by adsorption is intriguing but remains challenging. Herein, we present a starch-grafted-styrene hydrophilic porous resin (SGS-HPR) showing excellent BPs adsorption capacity, through simple graft copolymerization and then external knitting strategy. The typical influencing factors of graft copolymerization and external crosslinking processes were investigated systematically. A series of characterization experiments verified the successful fabrication of SGS-HPR and manifested that the optimum product, SGS-HPR$_7$, possesses a hierarchical porous structure with strong hydrophilicity. The abundant presence of starch chain in SGS-HPR$_7$, not only increased the hydrophilicity but also enhanced the adsorption affinity, making SGS-HPR$_7$ exhibit remarkable removal ability toward BPs. The adsorption performance of SGS-HPR$_7$ was studied systematically in static mode. The results showed that SGS-HPR$_7$ can adsorb BPs quickly with a stable ability irrespective of the varying aqueous environments. Besides, the continuous adsorption and regeneration experiments were conducted using bisphenol A (BPA) as the model BPs. The adsorbed BPA can be efficiently desorbed by ethanol elution, and the regenerated SGS-HPR$_7$ showed great recyclability. Interestingly, SGS-HPR$_7$ also retained the superior adsorption capacity and marvelous regeneration ability in the continuous adsorption experiments. Further, according to theoretical calculation studies, the hydrogen-bonding and π-π stacking interactions involved mechanism was uncovered clearly. Collectively, this work provides a new convenient strategy to fabricate new highly hydrophilic bio-based adsorbent for BPs removal.

1. Introduction

Bisphenols (BPs) having a wide range of industrial applications as plastic monomers and plasticizers are detected most frequently in various aquatic environments [1,2]. These emerging organic pollutants are also known as typical endocrine disruptors, which bring risks to aquatic organisms, animals, and human beings [3]. Thus, remediation of BPs contaminated water has received increasing attention from the related environmental scientific communities. Currently, kinds of technologies have been studied to remove BPs from aqueous solutions, including adsorption [4], membrane separation [5], photocatalytic degradation [6], biodegradation [7]. Among them, adsorption technology is a promising method to mitigate the BPs pollution in water due to its low-cost, high efficiency and simple methods of operation [8]. The fundamental and great challenge for adsorptive removing BPs from water is developing highly efficient adsorbents. Accordingly, various types of materials, such as carbon-based sorbents [9], metal organic framework [10,11], clay [12], porous silica [13] and porous organic polymers [14,15], have been developed for BPs adsorption.

As one important subclass of porous organic polymer, hypercrosslinked polymer (HCP) has attracted considerable interest for BPs removal because of its variable network structure, capability to trap small molecules and high physicochemical stability [16–18]. Of late, thanks to the Friedel-Craft alkylation based external crosslinking

* Corresponding authors: School of Chemistry and Chemical Engineering, Guangxi Key Laboratory of Petrochemical Resource Processing and Process Intensification Technology, Guangxi University, Nanning 530004, PR China (H. Ji).
E-mail addresses: chaikungang@gxu.edu.cn (K. Chai), jihb@mail.sysu.edu.cn (H. Ji).

https://doi.org/10.1016/j.cej.2021.132350
Received 31 May 2021; Received in revised form 16 August 2021; Accepted 5 September 2021
Available online 9 September 2021

method, various HCPs were synthesized using different aromatic blocks or monomers [19–21]. Among them, HCP knitted by polystyrene precursor with external crosslinker is most promising for industrial application due to its low cost, easy preparation and highly porous structure [22]. Thus, environmental remediation using polystyrene-based HCP as adsorbent has attracted considerable academic and engineering interests recently. However, the intrinsic hydrophobic property of the aromatic backbone adversely affects the polystyrene-based HCP dispersing in the aqueous phase during the adsorption process. More importantly, the discrepancy between hydrophilicity of BPs and hydrophobicity of polystyrene-based HCP can impede the interaction between BPs and adsorbent, resulting in low affinity of polystyrene-based HCP toward BPs. In term of these aspects, it is necessary to develop polystyrene-based HCP with dispersion ability in water and high affinity for BPs, which is crucial for large-scale deployment of BPs treatment process using polystyrene-based HCP as adsorbent.

Starch, one of the most abundant and inexpensive polysaccharides, is a typical natural matrix for fabricating bio-sorbent. Owing to the advantages of eco-friendliness, renewability and biodegradability, starch shows great potential in the bio-sorption field. Specifically, kinds of starch-based adsorbents, including crosslinked starch [23,24], etherification starch [25,26], esterification starch [27] and starch-graft-polymers [28,29], have been developed for removal of emerging organic pollutants from wastewater. Fundamentally speaking, the glucose units of starch shows special affinity toward the specific adsorbates through the intermolecular hydrogen bonding interaction, thereby exerting an important role for enhancing the adsorption capacity and selectivity. It is also worth noting that starch is more hydrophilic than another ubiquitous polysaccharide, cellulose, making starch as a more suitable candidate for construction of hydrophilic composite adsorbents.

Herein, to efficiently remove BPs from wastewater, we aim to fabricate starch-polystyrene based HCP, in which polystyrene-based HCP and starch will compensate for each other's limitations, i.e., hydrophobicity and poor porosity. More importantly, it is also anticipated that this porous composite can efficiently adsorb BPs through the synergistic effect of hydrogen bonds and π-π interactions. To this end, starch-grafted-styrene composite (SGS) was first obtained by simple graft copolymerization method. The swollen network of SGS was then crosslinked by the methylene group through the Friedel-Crafts alkylation, forming the permanent porosity. Owing to the imbedding of high hydrophilic starch chain, the as-prepared product exhibits strong water wet ability, so we define here as a starch-grafted-styrene composite hydrophilic porous resin (SGS-HPR). The synthesis procedure is shown in Scheme 1. To obtain the best performance of SGS-HPR, the typical influencing factors of graft copolymerization and external cross-linking process were investigated in turn. Through optimization, SGS-HPR with a hydrophilic surface and high specific surface area was obtained. We have validated the applicability of SGS-HPR as an efficient adsorbent for BPs by performing both batch and continuous column adsorption experiments. Due to the abundance of glucose and phenyl ring groups, favorable molecular interaction occurs when these groups are in contact with the BPs molecules, as demonstrated by the theoretical calculation. Interestingly, SGS-HPR can be regenerated and recycled in batch and continuous modes without much deterioration in the BPs removal efficiency.

2. Materials and methods

2.1. Materials

Soluble starch, sodium dodecyl sulfate (SDS), potassium persulfate (KPS), formaldehyde dimethyl acetal (FDA), 1,2-dichloroethane (DCE), bisphenol A (BPA), bisphenol AF (BPAF), bisphenol F (BPF), humic acid (HA) and bisphenol S (BPS) were purchased from Aladdin Chemistry Co., Ltd. (Shanghai, PR China). Anhydrous $FeCl_3$ was purchased from Adamas-beta Co., Ltd. Acetone, methanol, ethanol and ethyl acetate were analytical grade and sourced from Chengdu Kelong Chemical Reagent Factory, China. The wastewater was obtained from Huizhou Zhongxin Chemical Co., Ltd.

2.2. Preparation of SGS

SGS was prepared by emulsion free radical polymerization. In a typical protocol, 1 g of soluble starch was added to 20 mL of deionized water in a three-necked flask, followed by stirring mechanically (300 rpm) at 80 °C for 0.5 h to obtain gelatinized starch. Then, 0.12 g of KPS (3% of the total mass of starch and styrene), 0.48 g of SDS (2% of the total mass of the solution), and 3 g of styrene were added gradually into the mixture under nitrogen atmosphere. Polymerization was carried out at 80 °C with constant stirring kept at 300 rpm for 6 h. After polymerization, the reactant was cooled down, followed by adding ethanol to precipitate the product. The crude product was washed with ethanol and dried in an oven at 60 °C to constant weight. To remove the styrene homopolymers, the crude product was extracted with toluene for 6 h in a soxhlet extractor, followed by drying at 60 °C. SGS was recovered as a white powder. Besides, the values of grafting percentage *GP* (%) were calculated by Eq. (1) [30]:

$$GP(\%) = (m_1 - m_0)/m_0 \times 100\% \quad (1)$$

where m_0 and $m_1$is are the weights of starch (g) and SGS product (g), respectively.

In order to synthesize SGS with the highest value of *GP*, the influences of the dosage of the initiator, the mass ratio of styrene to starch and reaction time were investigated, respectively. The obtained SGSs were named as SGS-x_1%, SGS-x_2 and SGS-x_3h, where x_1, x_2 and x_3 were the percentage initiator concentration (based on total mass of starch and styrene), the mass ratio of styrene/starch and the reaction time (h), respectively.

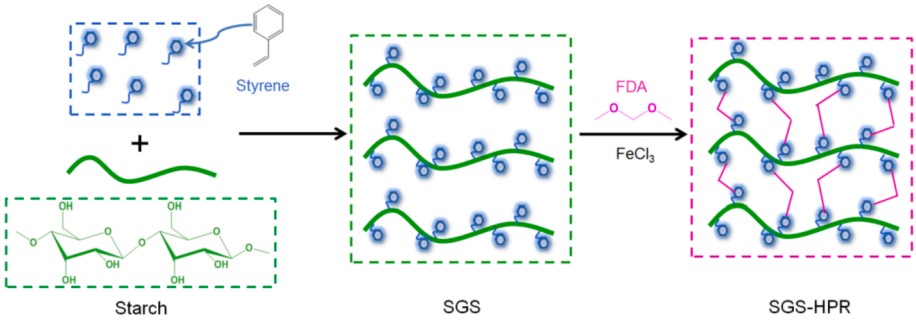

Scheme. 1. Synthesis procedure of SGS-HPR.

2.3. Preparation of SGS-HPR

In the second step, SGS-HPR was prepared following the external crosslinking protocol with SGS as the precursor and FDA as the crosslinker. Typically, 1 g of SGS (containing 6 mmol phenyl ring) and FDA (0.76 g, molar ratio of FDA to phenyl ring in SGS was 10/6) were added into 30 mL anhydrous DCE, and allowed to swell for 12 h at room temperature. Anhydrous $FeCl_3$ (1.62 g, the molar ratio of $FeCl_3$ to FDA was 1) was added into the mixture, and the reactant was stirred at 50 °C for 2 h and then at 80 °C for 10 h. During the entire reaction process, N_2 atmosphere and agitation at 300 rpm were maintained. After cooling to room temperature, the precipitate was washed with methanol until the filtrate became nearly colorless, followed by thorough washing with methanol by Soxhlet extraction for 24 h. The resulting yellow–brown SGS-HPR powder was collected after drying under vacuum at 60 °C for 24 h.

To optimize the synthesis procedure, both the reagent ratio and dosage of catalyst $FeCl_3$ were investigated in order. First, different molar ratios of FDA to phenyl ring in SGS (5/6, 10/6, 20/6 and 30/6) were utilized with the fixed molar ratio of $FeCl_3$/FDA (1/1), and the resulting materials were named as SGS-HPR_{y1} (y1 = 1–4). Then, the molar ratios of $FeCl_3$/FDA (0.5, 1.5, 2.5 and 3) were further studied when the molar ratio of FDA to benzene ring was 10/6, and we simply called these materials as SGS-HPR_{y2} (y2 = 5–8).

2.4. Characterization

Fourier transform infrared (FTIR) spectra were measured using a TENSOR II spectrometer (Bruker) in the range of 4000–400 cm^{-1} using KBr disks. The N_2 adsorption–desorption isotherms were carried out at −196 °C using an ASAP 2460 surface area and porosity analyzer (Micromeritics), and materials were degassed at 120 °C for 24 h. The solid-state ^{13}C CP/MAS NMR spectra were recorded on an AVANCE III spectrometer (Bruker). TG data were obtained on a NETZSCH TG-209 F3 instrument (NETZSCH, Germany) under N_2 atmosphere and in the temperature range of 30–800 °C at a heating rate of 10 °C min^{-1}. X-ray photoelectron spectroscopy (XPS) was performed in an electron spectrometer (ESCALAB 250 Thermo Fisher Scientific Inc., UK) equipped with a hemispherical sector energy analyzer, using a monochromatic Al Kα X-ray source. The granule morphology of samples was analyzed by a Hitachi SU-5000 scanning electron microscope (SEM). The transmission electron micrographs (TEM) were taken on Titan G260-300 (FEI) operating at 200 kV. The powder X-ray diffraction (XRD) data were obtained on a Smartlab-3kw diffractometer (Rigaku). The water contact angles were measured on DSA25 (KRUSS) to investigate hydrophilicity or hydrophobicity of the surface.

2.5. Batch adsorption experiments

BPs adsorption studies in batch mode were conducted using a 50 mL conical flask at 25 °C with the adsorbent dosage of 0.5 $g{\cdot}L^{-1}$ unless otherwise stated. The molecular structures of BPs used in the experiment is shown in Fig. S1, and the initial BPs concentration was set as 50–200 $mg{\cdot}L^{-1}$. In detail, 10 mg of adsorbent was contacted with 20 mL of BPs aqueous solution in a thermostatic shaker at 150 rpm for 12 h. The residual BPs concentration was measured from the UV–vis spectrophotometer (UV-2600, Shimadzu, Japan). The concentrations of different BPs in multiple solutes solution were determined by high performance liquid chromatography (HPLC) with a Shimadzu instrument (LC-16) with chromatographic column C18. Details for each individual adsorption experiment are given in Supplementary Information (Text S1).

The removal rate (R, %), equilibrium adsorption capacity (q_e, $mg{\cdot}g^{-1}$) and adsorption capacity at time t (q_t, $mg{\cdot}g^{-1}$) were calculated by Eq. (2), Eq. (3) and Eq. (4):

$$R(\%) = (C_0 - C_e)/C_0 \times 100 \quad (2)$$

$$q_e = (C_0 - C_e) \times V/m \quad (3)$$

$$q_t = (C_0 - C_t) \times V/m \quad (4)$$

where C_0, C_e and C_t are the initial concentrations, the equilibrium concentrations and the concentrations at time t, respectively. V (L) and m (g) are the volume of the solution and the mass of the adsorbent, respectively.

2.6. Continuous adsorption–desorption experiments

The continuous adsorption–desorption experiments were carried out in a water-jacketed glass column (inner diameter: 1.0 cm, length: 20.0 cm). Briefly, 1.5 g of SGS-HPR was swollen with pure water and packed into the glass column at 25 °C. A peristaltic pump (LONGING-pump, Type BF100C-1631Y) was used to ensure a constant flow rate of BPA aqueous solution (200 $mg{\cdot}L^{-1}$) at 6.0 $mL{\cdot}min^{-1}$. The concentration of BPA in the effluent (C_{ef}, $mg{\cdot}L^{-1}$) was continuously recorded until it was increased up to the feed concentration, and the breakthrough and saturation points were set at 5 % and 95 % of the influent BPA concentration, respectively.

After the dynamic adsorption, ethanol was applied for regeneration of the column with a constant flow rate of 1.0 $mL{\cdot}min^{-1}$ until no BPA was detected in the eluent, and then the column was further rinsed with water so as to the initial condition. The adsorption–desorption experiment of the column was repeated 3 times.

2.7. Computational methods

All theoretical calculations were carried out by density functional theory (DFT) at the level of M062X/6-31G* [31] using GAUSSIAN 16 software package. According to the characteristic results for the obtained products, an assumption was proposed that two structural units of SGS (one glucose unit grafted with one polystyrene unit) bridged through one methylene group represented the basic structure of SGS-HPR (as shown in Fig. S2). The interaction region and strength between SGS-HPR unit and BPA molecule were achieved by independent gradient model (IGM) isosurface analysis with Multiwfn 3.6 [32]. The IGM interaction regions and color mapped isosurface graphs of the electrostatic potential (ESP) were visualized by VMD 1.9.3 program [33]. The adsorption energy (E_{ads}) was obtained by calculating the energy difference before and after the adsorption of BPA onto SGS-HPR unit, which was calculated by Eq. (5) [34]:

$$E_{ads} = E_{total} - (E_{ad} + E_{sub}) \quad (5)$$

where E_{total}, E_{ad} and E_{sub} stand for the energies of complexes, adsorbent and substrate, respectively.

3. Results and discussion

3.1. Optimization of preparation conditions for SGS

In order to obtain SGS-HPR that exhibits ideal porosity, a high-level content of the grafted polystyrene in the precursor SGS, which facilitates the formation of rigid crosslink unit in the subsequent external crosslinking process, is expected. Therefore, the typical conditions for synthesizing SGS, including initiator concentration, mass ratio of styrene/starch and reaction time were investigated orderly. The rules for grafting polystyrene onto starch can be revealed clearly according to FTIR spectra of SGSs prepared under various conditions and the corresponding *GP* values (Fig. 1). Compared with the FTIR spectrum of starch (Fig. S3), SGSs not only retained the characteristic peaks of starch (such as ν_{O-H}, ν_{C-O-C}), but also displayed the characteristic peaks of the polystyrene structural unit (including $\nu_{C=C}$ and γ_{C-H} of the phenyl ring). In addition, the ν_{C-H} signal of SGSs FTIR spectra at 2923 cm^{-1} was also significantly enhanced, which was due to the insertion of the

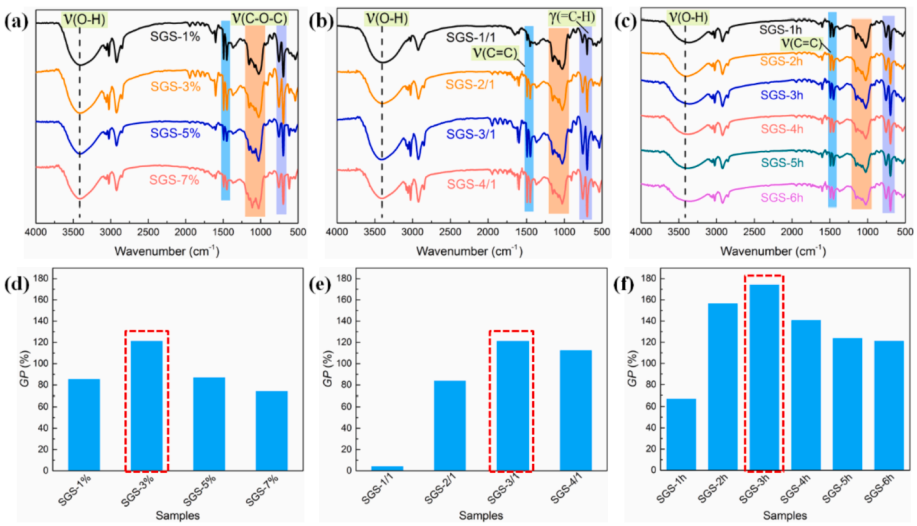

Fig. 1. (a-c) FTIR spectra of SGSs prepared under various conditions and (d-e) the corresponding *GP* values.

polystyrene backbone structure CH_2–CH_2 into the polymer network structure [30]. As shown in Fig. 1d, with increasing KPS percentage concentration, the *GP* values initially increased and then decreased gradually, similarly, the intensity of the characteristic peaks of the phenyl ring also exhibited the same tendency of initial increase followed by decreasing (Fig. 1a). The highest *GP* value was achieved when the KPS percentage concentration was 3%. The results showed that an optimum amount of KPS free radicals to attack the saccharide unit of starch, which would generate more starch radicals to react with styrene [35]. The influence of the mass ratio of styrene to starch on *GP* values was also investigated (Fig. 1e), *GP* values increased with increasing the mass ratio of styrene/starch from 1/1 to 3/1. When the mass ratio of styrene/starch was further increased to 4/1, the *GP* value decreased. The optimal mass ratio of styrene/starch was 3/1 and the characteristic peak intensity of benzene ring was strongest under this condition (Fig. 1b). Simultaneously, the effect of reaction time on the *GP* values was shown in Fig. 1f. It was obvious that the increase in the reaction time from 1 h to 3 h resulted in increasing in *GP* values, but when the reaction was run longer than 3 h, the *GP* values decreased. Additionally, the changing tendency for intensities of benzene ring characteristic peaks depicted in Fig. 1c were consistent with that of *GP* values. The reason may be that the concentrations of initiator and styrene monomer were high at the beginning of the reaction, but as the reaction proceeded the concentration decreased, which decreased the number of free radicals in the reaction system [36]. Based on the these results, SGS-3 h achieved the highest *GP* (174.2%) with the percentage KPS concentration, mass ratio of styrene/starch and reaction time are 3%, 3/1 and 3 h, respectively.

3.2. Optimization of preparation conditions for SGS-HPR

For fabricating SGS-HPR by external knitting strategy based on SGS, it was found that porosity of SGS-HPR could be easily tuned by varying the dosages of external cross-linker FDA and catalyst. Therefore, the influences of the two factors on the porosity were investigated in detail

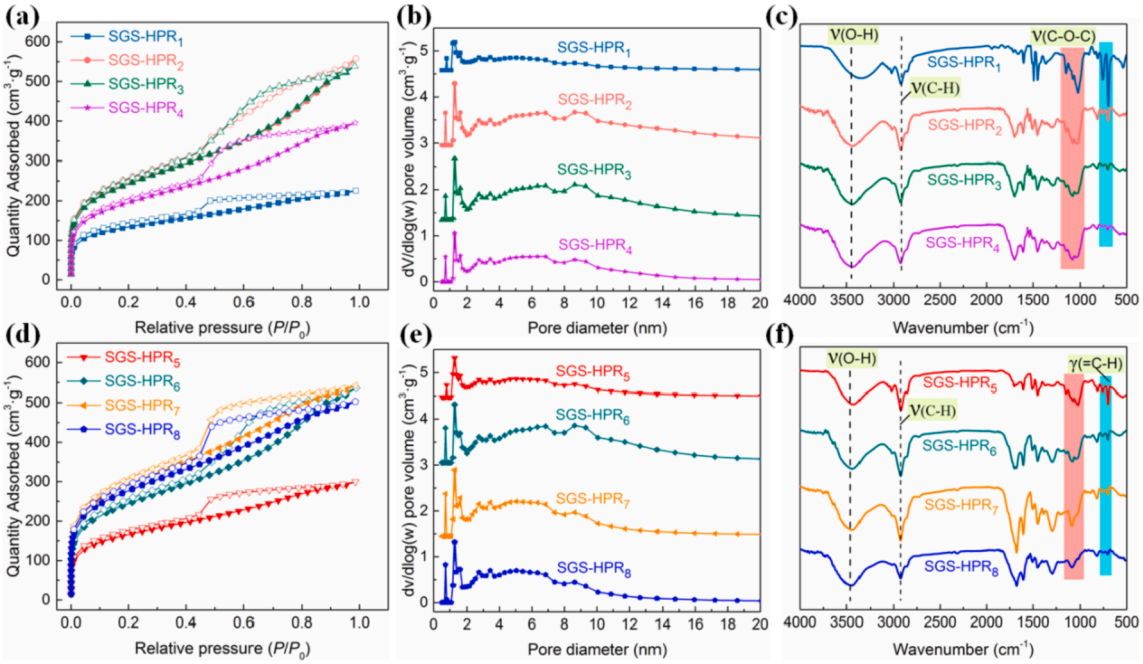

Fig. 2. The N_2 adsorption–desorption isotherms (a and d), pore size distribution curves (b and e), and FTIR spectra (c and f) of SGS-HPR_s.

(Fig. 2). We could observe that the N_2 adsorption–desorption isotherms of the SGS-HPR$_s$ prepared with different dosages of FDA exhibited a combination of type I and IV isotherms, which showed a sharp rise at low relative pressures demonstrating the presence of extensive microporous (Fig. 2a). Furthermore, the pore size distributions further confirmed the presence of micropores and mesopores (Fig. 2b). With the FDA dosage increasing, the BET surface area and pore volume of the obtained SGS-HPR$_s$ showed a trend of first increasing and then declining (Table 1). When the molar ratio of FDA to phenyl ring was 10/6, SGS-HPR$_2$ obtained the highest BET surface area of 863 $m^2 \cdot g^{-1}$. The FTIR spectra of the samples further verified this trend. As shown in Fig. 2c, the intensities of the mono-substituted phenyl ring $\gamma_{C\text{-}H}$ at 758 and 702 cm^{-1} significantly declined as increasing the FDA dosage. Furthermore, with increasing in the dosage of FDA, the characteristic peak of $\nu_{C\text{–}O\text{–}C}$ between 1200 and 950 cm^{-1} became broadened, indicating that the excessive FDA introduced methoxy groups among the network structure [19]. The insertion of methoxy groups occupied the pore volume of the product, thus deteriorating the porosity of SGS-HPR. Then, SGS-HPR$_s$ with a hierarchical pore structure can also be obtained by changing the dosage of catalyst. As shown in Fig. 2d and Table 1, both N_2 adsorption amount and specific surface area of SGS-HPR increased initially followed by decreasing with increasing the catalyst dosage, and SGS-HPR$_7$ possessed the highest porosity. Additionally, according to the pore size distribution curves (Fig. 2b and 2e), it is clear that SGS-HPR$_s$ contained abundant micropores and mesopores in their network. Conversely, the precursor polymer SGS exhibited typically nonporous structure according to its N_2 adsorption isotherm (Fig. S4) and the porous parameters listed in Table 1. So it can be inferred that the porous structure of SGS-HPR$_s$ was mainly introduced during the external crosslinking process. In addition, the FTIR spectra were also used to explain the changes in the crosslinking reaction under different catalyst dosages (Fig. 2f). As the dosage of catalyst increased, the intensity of the aliphatic $\nu_{C\text{–}H}$ at 2923 cm^{-1} increased first and then decreased. The intensity of this peak in SGS-HPR$_7$ was the strongest, which proved that the most methylene bridges were formed in the structure of SGS-HPR$_7$. Therefore, in the following structural analysis of samples, SGS-HPR$_7$ was used as a representative sample.

3.3. Structural analysis of SGS-HPR

To investigate the detailed information on the structure of SGS-HPR$_7$, several measurements were further performed. Firstly, the proposed grafting and external knitting processes for constructing SGS-HPR$_7$ was monitored by ^{13}C CP/MAS solid state NMR (Fig. 3a). Upon grafting polystyrene, the carbon peaks on the glucose unit of starch (C1-C6) were completely retained in the NMR spectrum of SGS. Meanwhile, the signals from non-substituted phenyl carbons (132 ppm), substituted phenyl carbons (150 ppm) and methylene-methylene carbons (40–60 ppm) appeared in the spectrum of SGS, indicating that the styrene structural unit was successfully grafted onto the starch molecular chain [37]. As for SGS-HPR$_7$, bridging between the phenyl rings of SGS precursor with methylene group can be confirmed by emergence of new resonance peak at 32 ppm. Furthermore, the peaks of non-substituted and substituted phenyl carbons were merged and shifted to the lower field. This was because the formation of methylene bridges led to an increased proportion of substituted phenyl carbons in SGS-HPR$_7$. In addition, the peak intensity of methylene-methylene carbons was enhanced and shifted to the lower field in the spectrum of SGS-HPR$_7$, which can be ascribed to the incorporation of methoxy groups inside the network. According to the above analysis, the results were consistent with the data of FTIR, which further confirmed the evolution process of SGS-HPR$_7$.

Table 1
Surface area and porous parameters of SGS and SGS-HPR$_s$.

Samples	S_{BET} ($m^2 \cdot g^{-1}$)	D_{ave} (nm)	S_{micro} ($m^2 \cdot g^{-1}$)	V_{total} ($cm^3 \cdot g^{-1}$)	V_{micro} ($cm^3 \cdot g^{-1}$)
SGS	0.93	\		0.02	\
SGS-HPR$_1$	481	2.82	158	0.29	0.06
SGS-HPR$_2$	863	3.76	196	0.71	0.08
SGS-HPR$_3$	858	3.72	181	0.69	0.08
SGS-HPR$_4$	690	3.42	150	0.51	0.07
SGS-HPR$_5$	591	3.04	160	0.39	0.07
SGS-HPR$_6$	870	3.67	209	0.71	0.09
SGS-HPR$_7$	1039	3.15	241	0.71	0.10
SGS-HPR$_8$	981	3.09	238	0.66	0.10

Then, the thermal stability of SGS-HPR$_7$ was analyzed in N_2 atmosphere. The TG-DTG curves of starch and SGS-HPR$_7$ were displayed in Fig. 3b. Compared with the single-step thermal degradation of raw starch, SGS-HPR$_7$ has multi-step thermal degradation starting at 200 °C, which is due to the different thermal stabilities of the different structural units in the composites. In addition, the residual specific gravity of SGS-HPR$_7$ at 800 °C is much higher than that of starch, which is mainly due to the higher carbon content of SGS-HPR$_7$, its denser and rigid crosslinking structures.

Insights into the evolution of surface chemical structure during the synthesis process were obtained by performing XPS characterization. As presented in Fig. 3c, the XPS survey spectra confirmed the existence of C and O elements in the samples, and the relative content of O element showed a trend of reducing at first and then increasing during the two-step preparation. This was owing to the fact that plenty of polystyrene chains were grafted onto the starch molecular chains during the grafting process (the C content increased sharply), and part of the FDA did not react completely so that a certain amount the methoxy groups were introduced into the cross-linking network structure during the further cross-linking process (the O content slightly increased). As shown in Fig. 3d, the high-resolution C1s spectrum of starch functional groups was divided into three peaks with binding energy of 284.7, 286.1 and 286.9 eV, which can be belonged to C atoms in C–C/C–H, C–O/C–OH and O–C–O, respectively [38,39]. Compared with high-resolution C1s spectrum of starch, SGS and SGS-HPR$_7$ showed C1s peak at 287.5 eV was assigned to C = O (carbonyl carbon). Moreover, the area percent of the peak at 284.7 eV were higher than that in starch, which was due to the presence of phenyl C = C (Fig. 3e-f and Table S1). On the other hand, the area percent of C-O/C-OH (8.49%) in SGS-HPR$_7$ is higher than SGS (6.35%) (Table S1), which was due to the presence of the methoxy groups. These results correlate well with the FTIR and ^{13}C NMR spectra, further confirming existence of a substantial amount of methoxy groups in the SGS-HPR$_7$ sample.

SEM and TEM were employed to study the morphological features of the samples. As shown in Fig. S5, starch exhibited spherical morphology, while styrene was further grafted onto starch, the surface of SGS became coarse and agglomerates appeared. After further external crosslinking between SGS phenyl rings with methylene bridges, the surface of SGS-HPR$_7$ was extremely loose and uneven, and displayed a porous structure (Fig. 4a). The SEM-EDS mappings evidently revealed the uniform distribution of the C and O elements on the surface of SGS-HPR$_7$ (Fig. 4c-e), which was in good agreement with the XPS survey spectra. Moreover, the formation of abundant and homogeneous pore structure of SGS-HPR$_7$ closely matching above N_2 adsorption–desorption results is further confirmed by the TEM image (Fig. 4b). XRD was used to study the crystal structures of the samples. As shown in Fig. S6, it was observed that the graft copolymerization reaction and crosslinking reaction destroyed the integrity of the polymer starch structure, the same with the observation of the previous report [40].

To investigate the hydrophilicity of SGS-HPR$_7$, the water contact

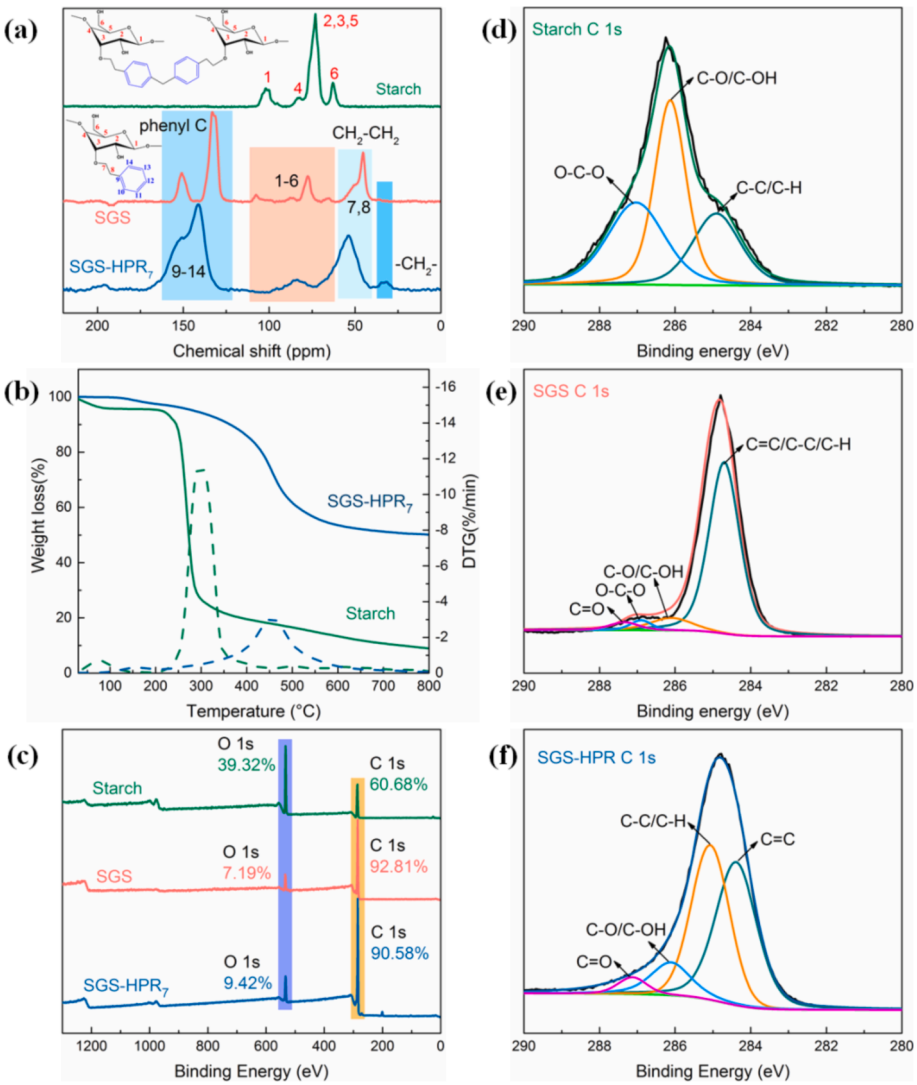

Fig. 3. (a) ^{13}C CP/MAS NMR spectra of starch, SGS and SGS-HPR$_7$, (b) TG of starch and SGS-HPR$_7$, (c) XPS survey spectra of starch, SGS and SGS-HPR$_7$, XPS C1s of (d) starch, (e) SGS and (f) SGS-HPR$_7$.

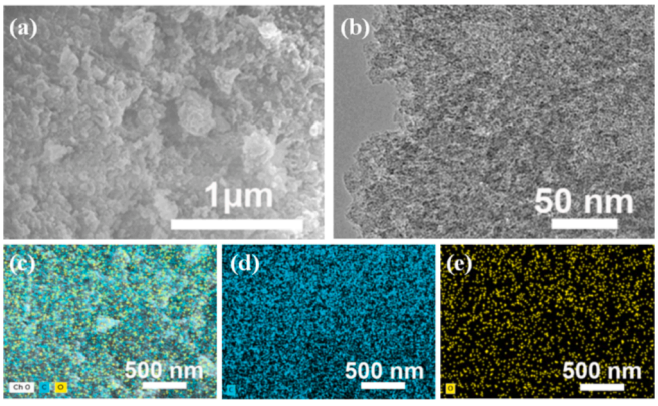

Fig. 4. (a) SEM and (b) TEM images of SGS-HPR$_7$, (c-e) SEM-EDS mapping images of SGS-HPR$_7$.

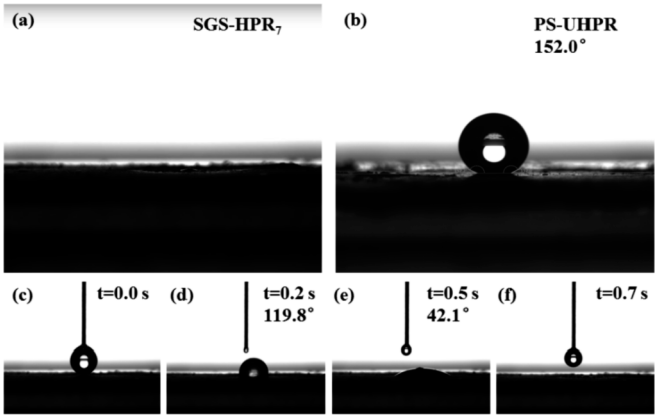

Fig. 5. Contact angle of (a and c-f) SGS-HPR$_7$ and (b) PS-UHPR.

angle on SGS-HPR$_7$ was measured. As shown in Fig. 5a, there is a nearly zero apparent contact angle for SGS-HPR$_7$, indicating a hydrophilic surface for SGS-HPR$_7$. We thus monitored the diffusion process of water upon contact with the surface of SGS-HPR$_7$ and found the quite fast and complete spreading of water drop in 0.7 s, illustrating that SGS-HPR$_7$ has a good water-wetting ability (Fig. 5c-f and video S1). In order to reflect the importance of the contribution of starch glucose units to hydrophilicity, a polystyrene ultrahydrophobic porous resin (PS-UHPR) was prepared under the same condition of SGS-HPR$_7$ with the absence of

starch. The contact angle of PS-UHPR is larger than 150.0° (Fig. 5b and video S2), suggesting that the polymer constructed with only polystyrene and FDA is a typical hydrophobic porous material, which is unfavorable to dispersion and adsorption in water. In a word, the good wetting ability and porous structure of SGS-HPR$_7$ provide the conditions for high capacity and rapid removal of BPs from water.

3.4. Batch adsorption performance

3.4.1. Screening of SGS-HPRs for BPs removal

In section 3.2, a series of SGS-HPRs with different crosslinking density and BET surface area were obtained by adjusting the dosage of FDA and catalyst. To evaluate the adsorption capacity of the obtained SGS-HPRs, adsorption experiments were carried out with four types of BPs and the results were shown in Fig. 6a. As expected, we found a clear positive correlation between the adsorption capacities of SGS-HPRs for BPs and their respective porosities. High porosity can facilitate the BPs diffusion and provide more adsorption sites, thus enhancing the capture ability toward BPs. Therefore, SGS-HPR$_7$ with the highest porosity possessed the superior adsorption capacity for BPs, which was chosen as the representative adsorbent subsequently.

To evaluate the potentiality of SGS-HPR$_7$ for efficient removal of BPs in their diluted solutions, we conducted a series of adsorption experiments in the BPs solutions with two low initial concentrations (500 and 1000 μg·L^{-1}). As can be seen in Fig. 6b, there is a high removal rate (greater than95%) by SGS-HPR$_7$ for all four BPs at these two low initial concentrations. Such excellent adsorption performance was mainly attributed to strong affinities of SGS-HPR$_7$ for BPs in the aqueous solution.

3.4.2. Adsorption kinetics

The time-dependent uptake amount of BPs on SGS-HPR$_7$ was recorded (Fig. 7a). It can be observed that the adsorption amount of BPs increased very rapidly during the first 30 min, after which the adsorption rate slowed down. The equilibrium adsorption time of BPA, BPAF, BPF and BPS was 150, 180, 80 and 120 min, respectively. The fast adsorption of BPs could be due to the existence of a large number of active sites and accessible diffusion pathway in the SGS-HPR$_7$, providing a strong driving force for the BPs molecule transportation from liquid phase to the surface of SGS-HPR$_7$. In addition, due to its strong affinity to water, SGS-HPR$_7$ can be quickly and completely dispersed in water, which greatly improved the external diffusion process and the adsorption rate at the beginning of adsorption. As the contact time increased, more and more active adsorption sites were occupied, the adsorption process reached plateau and the adsorption rates were limited by the larger diffusion resistance.

In order to better interpret the adsorption kinetics, pseudo-first order and pseudo-second order kinetic models were used to fit the adsorption data. The kinetic parameters and correlation coefficients (R^2) are summarized in Table S2. The high correlation coefficient of pseudo-second-order kinetic model for BPs indicates that the experimental data can be well described by pseudo-second-order kinetic model. Furthermore, the calculated values of adsorption capacity are closer to the experimental value for the pseudo-second kinetic order model as compared to the pseudo-first order kinetic model.

3.4.3. Adsorption isotherms and thermodynamics

The adsorption capacities as a function of substrates concentration are shown in Fig. 7b-e. It is observed that the adsorption capacity of SGS-HPR$_7$ increased with increasing initial concentration of BPs. The reason may be that the driving force of higher concentrations can promote the diffusion of BPs molecules into the pore channels [41]. Moreover, it is clearly observed that the adsorption capacity of SGS-HPR$_7$ descends with the increasing temperature, revealing that the adsorption process is favorable at low temperature. Further, the BPs adsorption behavior of SGS-HPR$_7$ was evaluated using Langmuir and Freundlich isotherm models. The correlative fitted plots of the two models are shown in Fig. 7b-e, and the related parameters are listed in Table S3. By comparing both models, the best fit for the Freundlich isotherm is obtained, indicating that the BPs adsorption proceeds on heterogeneous surface of SGS-HPR$_7$. In addition, the adsorption isotherms of BPs at 25 °C can also be well fitted by Langmuir isotherm model, and the q_m value of these BPs followed the descending order: BPAF (505.6 mg·L^{-1}) > BPA (443.8 mg·L^{-1}) > BPS (376.3 mg·L^{-1}) > BPF (352.0 mg·L^{-1}).

The thermodynamic studies can help us to explain the adsorption mechanism during the adsorption processes of BPs on SGS-HPR$_7$. According to the adsorption results at different temperatures, the adsorption thermodynamic parameters were calculated and displayed in Table S4. The negative values of ΔG^0 at all of three temperatures confirm that the adsorption progress is spontaneous. Moreover, the negative value of ΔH^0 indicates the adsorption progress is exothermic, which is consistent with the result that the adsorption is favorable at lower temperature. Finally, the positive value of ΔS^0 reflects that the increased of randomness at the solid–liquid interface during the adsorption process.

3.4.4. Effect of pH value and ionic strength

The influence of pH on BPs uptake was investigated in the range of pH 2–12. As shown in Fig. 8a, the adsorption capacities of BPA, BPF and BPS kept stable with increasing the pH from 2 to 10, followed by decreasing sharply with further increase of the initial pH to 12. For comparison, the stable-uptake pH range of another BPs analogue BPAF was a little narrower and the obvious decrease of BPAF uptake occurred at pH 10. The reason for the above changing trend was that most BPs molecules were negatively charged ionized because of ionization when the initial pH was greater than the pKa value (7.4–10.4) of BPs, which

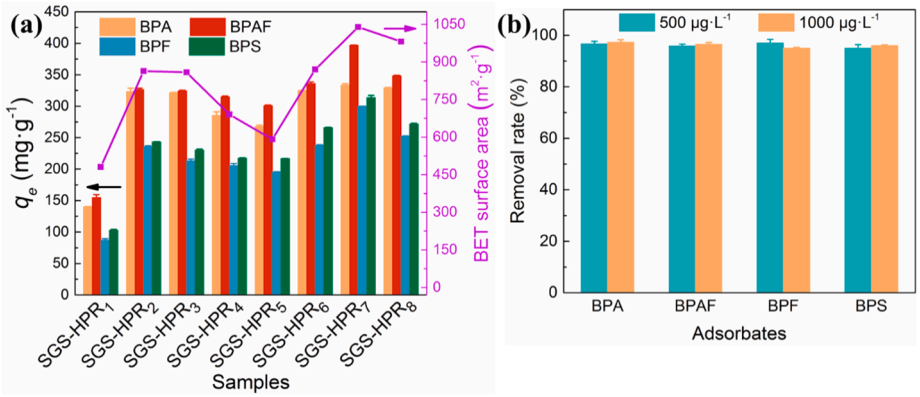

Fig. 6. (a) The adsorption capacity of BPs on SGS-HPR$_s$, (b) the removal rate of BPs on SGS-HPR$_7$ at the low initial concentrations (500 and 1000 μg·L^{-1}).

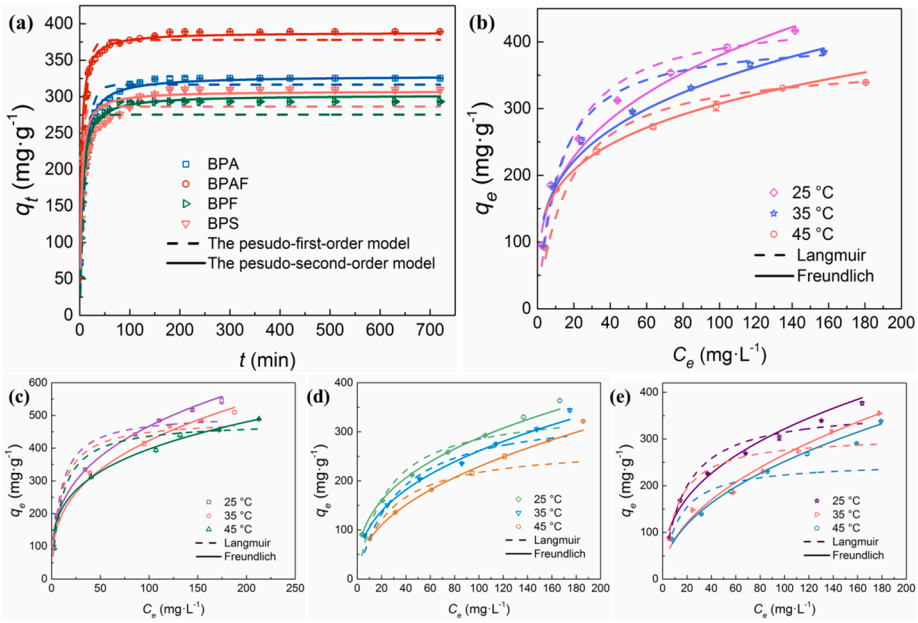

Fig. 7. (a) Fitting curves of adsorption kinetic of BPs onto SGS-HPR$_7$, (b-e) adsorption isotherms of BPA, BPAF, BPF and BPS onto SGS-HPR$_7$ at 25, 35 and 45 °C.

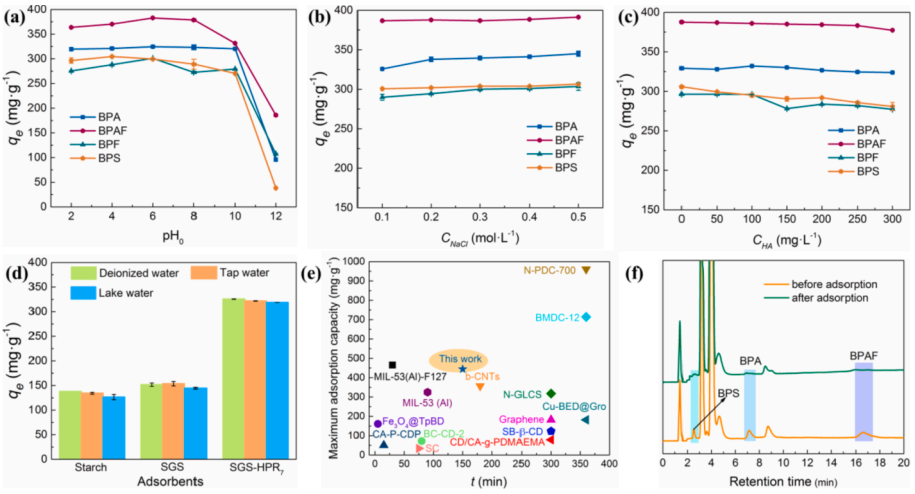

Fig. 8. The effects of (a) pH values, (b) ionic strength, (c) HA concentration and (d) the real water matrices, (e) comparison of maximum adsorption capacity from Langmuir model and equilibrium adsorption time for our prepared adsorbent with other reported novel adsorbents, Fe_3O_4@TpBD [44], CA-P-CDP [46], SC [47], BC-CD-2 [45], MIL-53(Al)-F127 and MIL-53(Al) [48], b-CNTs [49], N-GLCS [3], Graphene [4], SB-β-CD [50] and CD/CA-g-PDMAEMA [51], Cu-BED@Gro [52], BMDC-12 [53] and N-BDC-700 [54], (f) comparison the HPLC chromatograms of the waster sample before and after adsorption treatment by SGS-HPR$_7$.

led to the decrease of the hydrogen bond interactions between the BPs molecules and SGS-HPR$_7$ [42,43]. Further research on the adsorption capacity under different ionic strength was conducted (Fig. 8b). While the ionic strength ranging from 0.1 to 0.5 mol·L^{-1}, the adsorption capacity increased slightly at higher ionic strength was ascribed to the salting-out effect [44]. From the above results, SGS-HPR$_7$ maintains high adsorption efficiency for BPs over wide pH and ionic strength range.

3.4.5. *Effect of coexisting HA*

In the natural water system, natural organic matters (NOMs) commonly coexist with BPs. It is expected that the presence of NOMs would affect the removal efficiency of BPs. Herein, the effect of HA (a predominant NOM) was investigated for BPs removal. As can be seen from Fig. 8c, with increasing of the initial concentration of HA, the adsorption capacities of BPs only exhibited subtle decrement. Thus, it can be inferred that the coexisting HA scarcely competes with BPs for the adsorption sites, and SGS-HPR$_7$ can be used as an effective adsorbent for BPs removal.

3.4.6. *Competitive adsorption*

Generally, BPs pollutants rarely exist as sole solute in the real wastewater. So it's necessary to investigate the multicomponent adsorption performance of SGS-HPR$_7$. Here, the co-adsorption experiments were conducted in the equimolar quaternary solutions of the four BPs (each concentration was 50–200 mg·L^{-1}). As shown in Fig. S7, the uptake amount of each BPs was apparently lower than those in single-solute systems because of competition between the four BPs towards the adsorption sites. Compared with the other three BPs, BPAF showed superior adsorption in the competitive adsorption process, and the adsorption capacity order of four typical BPs is BPAF > BPA > BPF > BPS. Although competitive adsorption occurred in the co-adsorption process, the adsorption capacities of BPA kept gradually increasing with the increase of the initial concentration of the mixed solution, indicating that SGS-HPR$_7$ also possesses comparative selectivity toward BPA. Furthermore, given that BPA is the most ubiquitous endocrine disrupting chemical found in aquatic environments, BPA was selected as the representative BPs for further investigation of the adsorption performance of SGS-HPR$_7$.

3.4.7. Effect of the real water matrices

The effects of the two real water matrices (tap water and lake water) for the adsorption of BPA on SGS-HPR$_7$ were studied (Fig. 8d). Water quality information of the deionized water, tap water and lake water was shown in Table S5. It can be seen that from deionized water to lake water, the TOC content does not change significantly and the electric conductivity changes greatly, revealing that the organic matter content is relatively low but the ion concentration is higher in the real water matrices. Here, we noticed that the adsorption capacity of SGS-HPR$_7$ in the real water matrices was almost similar to that noted in deionized water, which was due to the higher ion concentration has little effect on the adsorption capacity of SGS-HPR$_7$. Irrespective of the difference of various ions, the organic matter content and pH in the real water matrices, the potential of SGS-HPR$_7$ to adsorb BPA was found to be superior. To investigate the structural effect of adsorbent on BPA uptake ability, starch and SGS were also used herein. It was worth noting that the adsorption capacities of SGS for BPA in the three real water matrices were slightly higher than that of starch, which was due to the introduction of a large number of benzene rings in grafting reaction to increase the adsorption sites. Meanwhile, the adsorption capacity of SGS-HPR$_7$ for BPA was significantly improved, which was related to its high porosity and much active adsorption sites. Based on the results, it is preliminarily determined that SGS-HPR$_7$ has double adsorption sites and a rich porous structure, which is the structural basis of its excellent adsorption performance.

3.4.8. Desorption and reusability studies

To determine the performance of solvent regeneration of the SGS-HPR$_7$, four common solvents, including methanol, ethanol, ethyl acetate and acetone were used to explore the desorption efficiency (*DE*, %) of BPA from SGS-HPR$_7$. As shown in Fig. S8a, a *DE* value of 91.97% was obtained with single elution of ethanol, which was much higher than that under the other three solvents. Also, the recovered BPA can be easily separated from ethanol and used for further applications. Therefore, ethanol was used to investigate the regeneration ability of SGS-HPR$_7$. Interestingly, after five recycles, SGS-HPR$_7$ retained its remarkable BPA adsorption capacity similar to the first use (Fig. S8b). Hence, this adsorbent shows exceptional reusability by mild regeneration for cost-effective wastewater treatment.

3.4.9. Adsorption performance comparison

Moreover, the adsorption performance of SGS-HPR$_7$ and other reported novel adsorbents for BPA were compared (Fig. 8e). Obviously, SGS-HPR$_7$ has higher adsorption capacity than most of the previously reported adsorbents (e.g., Fe_3O_4@TpBD [44], BC-CD-2 [45], and Graphene [4]). The reason should be that SGS-HPR$_7$ has high porosity and dual adsorption sites to provide sufficient active adsorption sites. In addition, SGS-HPR$_7$ can also adsorb BPA to achieve equilibrium in shorter time than most of these adsorbents, which may be attributed to its strong hydrophilicity and high porosity. Therefore, SGS-HPR$_7$ is an excellent absorbent for BPA removal in wastewater treatment.

3.4.10. Selective adsorption of BPs from wastewater

Use of SGS-HPR$_7$ for removing BPs from wastewater provides important guides for the practical application of the adsorbents in the real application. Therefore, one of the most commonly occurring industrial effluents was used for the preliminary study of the practical applicability of SGS-HPR$_7$ (see Text S1 for the detailed procedure). To illustrate the potential of SGS-HPR$_7$ for effective adsorption of BPs, Fig. 8f gives the LC chromatograms of raw wastewater and the treated wastewater by adsorption. In the raw wastewater, BPS, BPA and BPAF were identified at 2.5, 7.2 and 16.6 min by comparing the LC chromatogram of the standard substances (Fig. S9). Besides, unidentified peaks correspond to the main components of this wastewater which coexisted with BPs. A comparison of the chromatograms in Fig. 8f shows that the peaks of BPA and BPAF disappeared after adsorption, and the peak intensity of BPS was also weakened significantly. These results indicated that the effective adsorption of BPs on the SGS-HPR$_7$. Meantime, the peak intensities of other organic substances remained unchanged, suggesting they were scarcely removed. Additionally, the organic content of wastewater was monitored by TOC analysis. A small decrease of the TOC contents in wastewater after adsorption (from 232.9 to 230.6 mg·L^{-1}) further proved the excellent adsorption selectivity of SGS-HPR$_7$ to BPs. Further practical application of SGS-HPR$_7$ will be conducted in the future research.

3.5. Continuous adsorption performance

To test the efficacy of SGS-HPR$_7$ under flow-through conditions, fixed-bed column was packed with the SGS-HPR$_7$ particles and tested for BPA adsorption. The experimental breakthrough curves of BPA adsorption onto SGS-HPR$_7$ were shown in Fig. 9a. During the initial stage, BPA was completely adsorbed because the fresh SGS-HPR$_7$ had sufficient active sites, resulting in collection of pure water in the column outlet. With the adsorption site being occupied gradually by BPA, the breakthrough point occurred at ca. 2520 mL, after which the BPA concentration in the effluent quickly increased until attained the inlet concentration, yielding a sharp breakthrough curve. After adsorption saturation, ethanol was applied for regenerating the exhausted fixed-bed. As shown in Fig. 9b, a sharp desorption peak (with 1355 mg·L^{-1} of maximum BPA concentration in the eluate) was observed during the initial desorption process, and it can be seen that 360 mL of ethanol was sufficient to completely desorb the adsorbed BPA from the column. In addition, continuous adsorption-regeneration experiments were repeated for 3 cycles to test reusability of SGS-HPR$_7$, nearly identical breakthrough curves were observed in the recycling adsorption experiments. In order to fundamentally explore dynamic adsorption performance of SGS-HPR$_7$, Thomas model (parameters were listed in Text S2) was adopted to fit the three breakthrough curves. As illustrated in Fig. S10, the breakthrough curves of BPA can be well described by the Thomas model. And the calculated equilibrium adsorption capacities in the three cycles (Table S6) were in good agreement with those predicted using the Langmuir model, confirming that SGS-HPR$_7$ would be an efficient and stable adsorbent for the removal of BPA both in batch and continuous modes.

4. Adsorption mechanism

The quantum-chemical calculation studies have been undertaken to understand the favorable interactions between the BPA and SGS-HPR. By analyzing electrostatic potential of BPA and SGS-HPR unit (Fig. S2), it could be seen that the π electron clouds of the phenyl ring and the glucose unit were the main potential adsorption sites. The optimized geometries of BPA molecule adsorbed on the above two adsorption sites are shown in Fig. 10. It can be seen that the regional isosurface (IGM) of BPA on phenyl ring site was clearly green in color, indicating there mainly existed weak interactions (such as π-π stacking and van der Waals interaction) between BPA molecule and phenyl ring site. By comparison, both the blue and green colors were observed in the IGM of BPA on glucose unit, which was indicative of formation of strong interaction between BPA molecule and glucose unit (e.g., hydrogen bond). This observation was in consistent with that the corresponding E_{ads} of BPA onto glucose unit was higher than that of BPA onto the phenyl ring (Fig. 10c). Further, we have applied Multiwfn to analyze the energy decomposition based on AMBER molecular force field (Fig. 10c). It can be seen that dispersion interaction (π-π stacking) primarily contributed E_{ads} of BPA onto phenyl ring. While, the electrostatic interaction (hydrogen bond) and dispersion interaction altogether contributed to a higher E_{ads} of BPA on the glucose unit.

Based on the above experimental and theoretical results, we can infer that the porous structure can accommodate large amount of BPA molecules, more importantly, the phenyl ring and glucose unit cooperate to

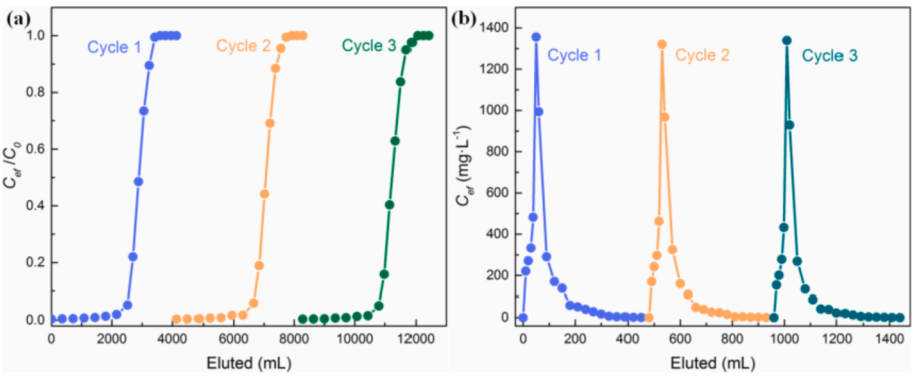

Fig. 9. (a) Experimental breakthrough curves for adsorption of BPA aqueous solution on SGS-HPR$_7$, (b) regeneration of SGS-HPR$_7$ loaded with BPA.

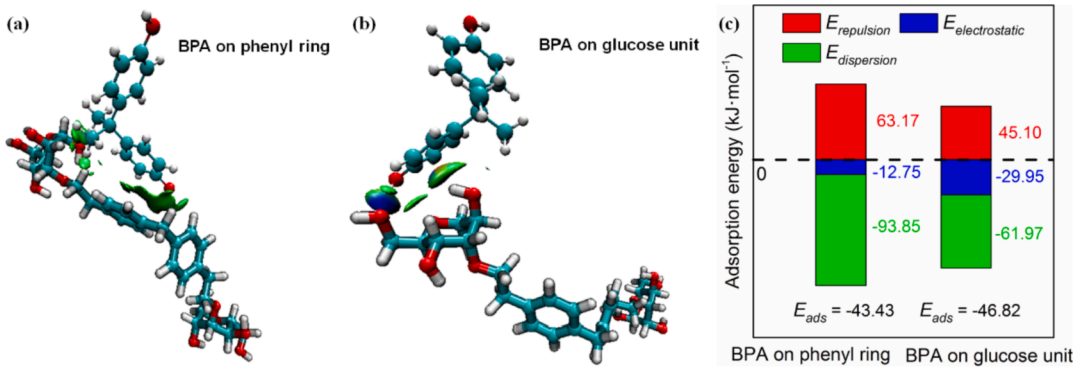

Fig. 10. Optimized BPA adsorbed on phenyl ring (a) and (b) glucose unit of SGS-HPR$_7$ and (c) their corresponding adsorption energies and energy decomposition analysis based on AMBER molecular force field. Illustration of the dispersed IGM isosurface was set to 0.003. In general, the blue, green, and red colors indicated the strong attraction, the van der Waals interaction and the repulsion force, respectively.

bind BPA molecules. On one hand, a large number of hydroxyl groups have been confirmed on the surface of SGS-HPR due to the abundance of glucose units, hydrogen bonding interaction between the –OH groups on BPA and –OH groups on SGS-HPR could play an important role in the adsorption process. On the other hand, both BPA molecule and SGS-HPR$_7$ owned sufficient aromatic units, the π–π stacking interactions between them could facilitate the migration of BPA to the SGS-HPR, resulting in an improvement on adsorption. The above mentioned reasons explained that the adsorption mechanisms between the BPA and SGS-HPR involved the synergism of hydrogen-bonding interactions and π-π stacking interactions (Fig. 11). The presence of abundant binding sites with high energies contributes to the extraordinary uptake of BPA on SGS-HPR.

5. Conclusions

To remove BPs in water, this work describes the synthesis of an effective starch based adsorbent, SGS-HPR, using polystyrene grafting and subsequent external crosslinking protocol. In optimized preparation conditions, SGS-HPR$_7$ was obtained with hierarchical porosity and high surface area of 1039 m^2·g^{-1}, significantly favoring the adsorption process of BPs onto the active sites. From the various characteristic results, the presence of starch chain, crosslinked polystyrene units with methylene bridges, and a substantial amount of methoxy groups in the network of SGS-HPR$_7$ were confirmed, respectively. Moreover, the water contact angle test proved the strong hydrophilicity of SGS-HPR$_7$, which is critical for quickly transferring BPs from the solution onto the surface of adsorbent. Due to the abundant existence of glucose units and phenyl rings in the porous structure, SGS-HPR$_7$ possessed superior ability to remove BPs from water. Moreover, the recyclability of SGS-HPR$_7$ was also verified by adsorption–desorption recycle experiments

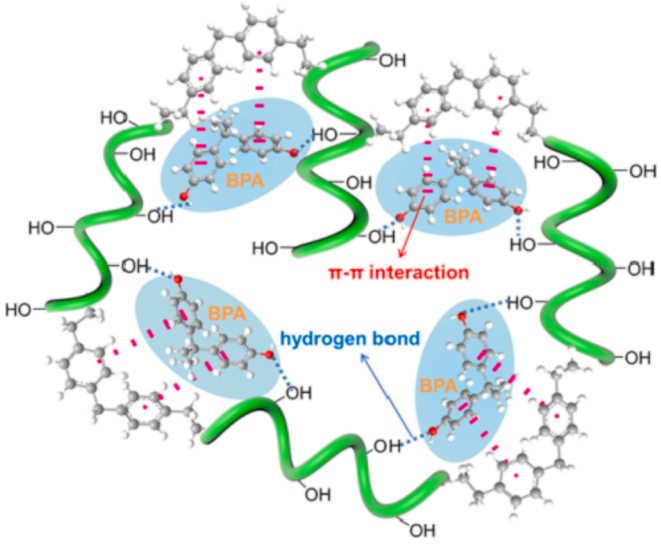

Fig. 11. The proposed adsorption mechanism of BPA onto SGS-HPR$_7$.

both in batch and continuous modes. Meanwhile, the complete removal of BPs in the real wastewater sample verified the feasibility of SGS-HPR$_7$ for the practical application. Further, the adsorption mechanism mainly involving the synergism of hydrogen-bonding and π-π stacking interactions was proved by theoretical calculations. Based on above analysis, here we provided a new simple protocol to fabricate hydrophilic starch based HCPs, which can be applied for removal of BPs from aqueous solutions.

Declaration of Competing Interest

The authors declare that they have no known competing financial interests or personal relationships that could have appeared to influence the work reported in this paper.

Acknowledgements

This work was supported by National Natural Science Foundation of China (21868002 and 21961160741), the Natural Science Foundation of Guangxi Province (No. 2018GXNSFAA281206, No. 2020GXNSFGA297001 and No. 2020GXNSFAA297044), Key R & D projects of Guangxi Province (AB20238010), special funding for 'Guangxi Bagui Scholars', and Guangxi scholarship fund for the middle-aged backbone teachers. The theoretical calculations were done using the computing facilities of the High Performance Computing Center in Guangxi University.

Appendix A. Supplementary data

Supplementary data to this article can be found online at https://doi.org/10.1016/j.cej.2021.132350.

References

[1] J.R. Rochester, A.L. Bolden, Bisphenol S and F: A systematic review and comparison of the hormonal activity of bisphenol A substitutes, Environ. Health Perspect. 123 (2015) 643–650.
[2] J.I. Cacho, N. Campillo, P. Viñas, M. Hernández-Córdoba, Stir bar sorptive extraction coupled to gas chromatography-mass spectrometry for the determination of bisphenols in canned beverages and filling liquids of canned vegetables, J. Chromatogr. A 1247 (2012) 146–153.
[3] P.Y. Xiao, P. Wang, H.M. Li, Q.Y. Li, Y.P. Shi, X.L. Wu, H.J. Lin, J.R. Chen, X. K. Wang, New insights into bisphenols removal by nitrogen-rich nanocarbons: Synergistic effect between adsorption and oxidative degradation, J. Hazard. Mater. 345 (2018) 123–130.
[4] J. Xu, L.i. Wang, Y. Zhu, Decontamination of bisphenol A from aqueous solution by graphene adsorption, Langmuir 28 (22) (2012) 8418–8425.
[5] Y. Zhang, C. Causserand, P. Aimar, J.P. Cravedi, Removal of bisphenol A by a nanofiltration membrane in view of drinking water production, Water Res. 40 (20) (2006) 3793–3799.
[6] C. Wang, L. Zhu, C. Song, G. Shan, P. Chen, Characterization of photocatalyst $Bi_{3.84}W_{0.16}O_{6.24}$ and its photodegradation on bisphenol A under simulated solar light irradiation, Appl Catal B-Environ 105 (1-2) (2011) 229–236.
[7] E. Danzl, K. Sei, S. Soda, M. Ike, M. Fujita, Biodegradation of bisphenol A, bisphenol F and bisphenol S in seawater, Int. J. Environ. Res. Public Health 6 (4) (2009) 1472–1484.
[8] A. Leudjo Taka, M.J. Klink, X. Yangkou Mbianda, E.B. Naidoo, Chitosan nanocomposites for water treatment by fixed-bed continuous flow column adsorption: A review, Carbohydr. Polym. 255 (2021) 117398–117399.
[9] Y.C. Gong, J.B. Su, M.Y. Li, A.X. Zhu, G.S. Liu, P.Y. Liu, Fabrication and adsorption optimization of novel magnetic core-shell chitosan/graphene oxide/beta-cyclodextrin composite materials for bisphenols in aqueous solutions, Materials 13 (2020) 19.
[10] Y. Yuan, X.W. Zheng, H.Z. Lin, Y.Y. Li, M. Yang, X.L. Liu, C.H. Deng, Z.Q. Fan, Development of a hydrophilic magnetic amino-functionalized metal-organic framework for the highly efficient enrichment of trace bisphenols in river water samples, Talanta 211 (2020) 10.
[11] A.N. Meng, L.X. Chaihu, H.H. Chen, Z.Y. Gu, Ultrahigh adsorption and singlet-oxygen mediated degradation for efficient synergetic removal of bisphenol A by a stable zirconium-porphyrin metal-organic framework, Sci Rep 7 (2017) 9.
[12] W.T. Vieira, M.B. de Farias, M.P. Spaolonzi, M.G.C. da Silva, M.G.A. Vieira, Removal of endocrine disruptors in waters by adsorption, membrane filtration and biodegradation. A review, Environ. Chem. Lett. 18 (2020) 1113–1143.
[13] W. Teng, Z. Wu, D. Feng, J. Fan, J. Wang, H. Wei, M. Song, D. Zhao, Rapid and efficient removal of microcystins by ordered mesoporous silica, Environ. Sci. Technol. 47 (15) (2013) 8633–8641.
[14] W.Y. He, X.Y. Ren, Z.Q. Yan, J. Wang, L.H. Lu, Porous beta-cyclodextrin nanotubular assemblies enable high-efficiency removal of bisphenol micropollutants from aquatic systems, Nano Res. 13 (2020) 1933–1942.
[15] L.J. You, K. Xu, G.J. Ding, X.M. Shi, J.M. Li, S.Y. Wang, J.B. Wang, Facile synthesis of Fe_3O_4@COF covalent organic frameworks for the adsorption of bisphenols from aqueous solution, J. Mol. Liq. 320 (2020) 10.
[16] X. Wang, H. Li, J. Huang, Adsorption of p-chlorophenol on three amino-modified hyper-cross-linked resins, J. Colloid Interface Sci. 505 (2017) 585–592.
[17] M. Ghafari, Y.B. Cui, A. Mali, J.D. Atkinson, Phenol adsorption and desorption with physically and chemically tailored porous polymers: Mechanistic variability associated with hyper-cross-linking and amination, J. Hazard. Mater. 361 (2019) 162–168.
[18] Q. Wang, L. Zhang, L. Hao, C. Wang, Q. Wu, Z. Wang, Phosphorous-enriched knitting aryl network polymer for the rapid and effective adsorption of aromatic compounds, J. Chromatogr. A 1575 (2018) 18–25.
[19] L. Tan, B. Li, X. Yang, W. Wang, B. Tan, Knitting hypercrosslinked conjugated microporous polymers with external crosslinker, Polymer 70 (2015) 336–342.
[20] Y.W. Yang, L.Y. Feng, J. Ren, Y.F. Liu, S.B. Jin, L. Su, C. Wood, B.E. Tan, Soluble hyperbranched porous organic polymers, Macromol. Rapid Commun. 39 (2018) 7.
[21] L.X. Tan, B.E. Tan, Functionalized hierarchical porous polymeric monoliths as versatile platforms to support uniform and ultrafine metal nanoparticles for heterogeneous catalysis, Chem. Eng. J. 390 (2020) 11.
[22] M.P. Tsyurupa, V.A. Davankov, Porous structure of hypercrosslinked polystyrene: State-of-the-art mini-review, React. Funct. Polym. 66 (7) (2006) 768–779.
[23] L. Guo, G. Li, J. Liu, Y. Meng, Y. Tang, Adsorptive decolorization of methylene blue by crosslinked porous starch, Carbohydr. Polym. 93 (2) (2013) 374–379.
[24] M. Haroon, L.i. Wang, H. Yu, N.M. Abbasi, Z.-u.-A. Zain-ul-Abdin, M. Saleem, R. U. Khan, R.S. Ullah, Q. Chen, J. Wu, Chemical modification of starch and its application as an adsorbent material, RSC Adv. 6 (82) (2016) 78264–78285.
[25] Q. Chen, H. Yu, L.i. Wang, Z. ul Abdin, Y. Chen, J. Wang, W. Zhou, X. Yang, R. U. Khan, H. Zhang, X. Chen, Recent progress in chemical modification of starch and its applications, RSC Adv. 5 (83) (2015) 67459–67474.
[26] T. Heinze, V. Haack, S. Rensing, Starch derivatives of high degree of functionalization. 7. Preparation of cationic 2-hydroxypropyl trimethylammonium chloride starches, Starch-Starke 56 (7) (2004) 288–296.
[27] X. Yan, M. Diao, Y. Yu, F. Gao, E. Wang, Z. Wang, T. Zhang, Influence of esterification and ultrasound treatment on formation and properties of starch nanoparticles and their impact as a filler on chitosan based films characteristics, Int. J. Biol. Macromol. 179 (2021) 154–160.
[28] J.C. Cazotti, A.T. Fritz, O. Garcia-Valdez, N.M.B. Smeets, M.A. Dube, M. F. Cunningham, Graft modification of starch nanoparticles using nitroxide-mediated polymerization and the grafting from approach, Carbohydr. Polym. 228 (2020) 9.
[29] L. Wang, J. Shen, Y. Men, Y. Wu, Q. Peng, X. Wang, R. Yang, K. Mahmood, Z. Liu, Corn starch-based graft copolymers prepared via ATRP at the molecular level, Polym. Chem. 6 (18) (2015) 3480–3488.
[30] K. Kaewtatip, V. Tanrattanakul, Preparation of cassava starch grafted with polystyrene by suspension polymerization, Carbohydr. Polym. 73 (4) (2008) 647–655.
[31] E. Ruiz, Exchange coupling constants using density functional theory: The M0X suite, Chem. Phys. Lett. 460 (1-3) (2008) 336–338.
[32] T. Lu, F. Chen, Multiwfn: A multifunctional wavefunction analyzer, J. Comput. Chem. 33 (2012) 580–592.
[33] W. Humphrey, A. Dalke, K. Schulten, VMD: Visual molecular dynamics, J. Mol. Graphics 14 (1996) 33–38.
[34] D.L. Wei, C.F. Zhao, A. Khan, L. Sun, Y.F. Ji, Y.J. Ai, X.K. Wang, Sorption mechanism and dynamic behavior of graphene oxide as an effective adsorbent for the removal of chlorophenol based environmental-hormones: A DFT and MD simulation study, Chem. Eng. J. 375 (2019) 11.
[35] V. Nikolic, S. Velickovic, A. Popovic, Influence of amine activators and reaction parameters on grafting reaction between polystyrene and starch, J. Polym. Res. 21 (2014) 10.
[36] M.-C. Li, X. Ge, U.R. Cho, Emulsion grafting vinyl monomers onto starch for reinforcement of styrene-butadiene rubber, Macromol. Res. 21 (5) (2013) 519–528.
[37] R.V. Law, D.C. Sherrington, C.E. Snape, I. Ando, H. Kurosu, Solid-state ^{13}C MAS NMR studies of hyper-cross-linked polystyrene resins, Macromolecules 29 (19) (1996) 6284–6293.
[38] R. Kumar, J. Rashid, M.A. Barakat, Synthesis and characterization of a starch–AlOOH–FeS_2 nanocomposite for the adsorption of congo red dye from aqueous solution, RSC Adv. 4 (72) (2014) 38334–38340.
[39] A. Uliniuc, M. Popa, E. Drockenmuller, F. Boisson, D. Leonard, T. Hamaide, Toward tunable amphiphilic copolymers via CuAAC click chemistry of oligocaprolactones onto starch backbone, Carbohydr. Polym. 96 (1) (2013) 259–269.
[40] Q. Zhang, Z. Wang, C. Zhang, R.E. Aluko, J. Yuan, X. Ju, R. He, Structural and functional characterization of rice starch-based superabsorbent polymer materials, Int. J. Biol. Macromol. 153 (2020) 1291–1298.
[41] Z.-D. Du, Y.-Y. Cui, C.-X. Yang, X.-P. Yan, Core–shell magnetic amino-functionalized microporous organic network nanospheres for the removal of tetrabromobisphenol A from aqueous solution, ACS Appl Nano Mater 2 (3) (2019) 1232–1241.
[42] Z. Wang, S. Guo, B. Zhang, J. Fang, L. Zhu, Interfacially crosslinked β-cyclodextrin polymer composite porous membranes for fast removal of organic micropollutants from water by flow-through adsorption, J. Hazard. Mater. 384 (2020), 121187.
[43] M.V. López-Ramón, R. Ocampo-Pérez, M.I. Bautista-Toledo, J. Rivera-Utrilla, C. Moreno-Castilla, M. Sánchez-Polo, Removal of bisphenols A and S by adsorption on activated carbon clothes enhanced by the presence of bacteria, Sci. Total Environ. 669 (2019) 767–776.
[44] Y. Li, C.-X. Yang, X.-P. Yan, Controllable preparation of core-shell magnetic covalent-organic framework nanospheres for efficient adsorption and removal of bisphenols in aqueous solution, Chem. Commun. 53 (16) (2017) 2511–2514.
[45] F. Liu, C. Chen, J. Qian, Film-like bacterial cellulose/cyclodextrin oligomer composites with controllable structure for the removal of various persistent organic pollutants from water, J. Hazard. Mater. 405 (2021) 124122, https://doi.org/10.1016/j.jhazmat.2020.124122.

[46] Y.C. Lv, J.C. Ma, K.Y. Liu, Y.T. Jiang, G.F. Yang, Y.F. Liu, C.X. Lin, X.X. Ye, Y.Q. Shi, M.H. Liu, L.H. Chen, Rapid elimination of trace bisphenol pollutants with porous beta-cyclodextrin modified cellulose nanofibrous membrane in water: Adsorption behavior and mechanism, J. Hazard. Mater. 403 (2021) 14.
[47] M.H. Dehghani, M. Ghadermazi, A. Bhatnagar, P. Sadighara, G. Jahed-Khaniki, B. Heibati, G. McKay, Adsorptive removal of endocrine disrupting bisphenol A from aqueous solution using chitosan, J. Environ. Chem. Eng. 4 (3) (2016) 2647–2655.
[48] M. Zhou, Y.-N. Wu, J. Qiao, J. Zhang, A. McDonald, G. Li, F. Li, The removal of bisphenol A from aqueous solutions by MIL-53(Al) and mesostructured MIL-53(Al), J. Colloid Interface Sci. 405 (2013) 157–163.
[49] P. Wang, P. Xiao, S. Zhong, J. Chen, H. Lin, X.-L. Wu, Bamboo-like carbon nanotubes derived from colloidal polymer nanoplates for efficient removal of bisphenol A, J. Mater. Chem. A 4 (40) (2016) 15450–15456.
[50] F.M. Mpatani, A.A. Aryee, A.N. Kani, Q. Guo, E. Dovi, L. Qu, Z. Li, R. Han, Uptake of micropollutant-bisphenol A, methylene blue and neutral red onto a novel bagasse-β-cyclodextrin polymer by adsorption process, Chemosphere 259 (2020), 127439.
[51] Y. Zhou, Y. Hu, W. Huang, G. Cheng, C. Cui, J. Lu, A novel amphoteric β-cyclodextrin-based adsorbent for simultaneous removal of cationic/anionic dyes and bisphenol A, Chem. Eng. J. 341 (2018) 47–57.
[52] M.A. Ahsan, V. Jabbari, M.T. Islam, R.S. Turley, N. Dominguez, H. Kim, E. Castro, J.A. Hernandez-Viezcas, M.L. Curry, J. Lopez, J.L. Gardea-Torresdey, J.C. Noveron, Sustainable synthesis and remarkable adsorption capacity of MOF/graphene oxide and MOF/CNT based hybrid nanocomposites for the removal of bisphenol A from water, Sci. Total Environ. 673 (2019) 306–317.
[53] B.N. Bhadra, J.K. Lee, C.W. Cho, S.H. Jhung, Remarkably efficient adsorbent for the removal of bisphenol A from water: Bio-MOF-1-derived porous carbon, Chem. Eng. J. 343 (2018) 225–234.
[54] J.M. Park, S.H. Jhung, Remarkable adsorbent for removal of bisphenol A and S from water: Porous carbon derived from melamine/polyaniline, Chemosphere 268 (2021), 129342.